Processing and Application of Ceramics 19 [2] (2025) 128–138
https://doi.org/10.2298/

Green synthesis of $Ba(Fe_{1/2}Nb_{1/2})O_3$ ceramics with high dielectric constant

Anal K. Jha[1], Kamal Prasad[2,*]

[1] *University Department of Chemistry, T.M. Bhagalpur University, Bhagalpur 812007, India*
[2] *University Department of Physics, T.M. Bhagalpur University, Bhagalpur 812007, India*

Received 28 January 2025; Received in revised form 23 March 2025; Accepted 21 May 2025

Abstract

Domestic and/or kitchen wastes are a burden to the environment and they attract microbes after gradual festering and decomposition adding to the deterioration of the ambient air quality. Waste lemon peels are one of them. In this work, a novel green, reproducible and cost-effective synthetic method for the fabrication of dielectric $Ba(Fe_{1/2}Nb_{1/2})O_3$ *(abbreviated as n-BFN) nanopowder mediated by waste lemon peel is presented. The waste lemon peels are inundated in promising secondary metabolites, each having its own potential in nanopowder preparation. The lemon peels are rich in terpenoids, ascorbic acid, citric acid along with other metabolites which in consonance help to ensure the synthesis of nanoscale compounds. A plausible mechanism for the green synthesis process in n-BFN formation is proposed. X-ray diffraction analyses confirmed the formation of a single-phase BFN with cubic structure (a = 4.0597 Å, space group* $Pm\bar{3}m$*). Transmission and scanning electron microscopy images revealed both individual nanoparticles and a few aggregates whose sizes varied between 11 and 48 nm. The complex impedance and electric modulus spectroscopy indicated the dielectric relaxation to be of the non-Debye type. The correlated barrier hopping model was used to favourably explain the mechanism of charge transport within the material. Additionally, the prepared n-BFN exhibited a high dielectric constant (~10^4) and a low tangent loss (0.35) at room temperature, making them promising candidate for microelectronic applications. Magnetic studies of the n-BFN (coercive field of 126 Oe, retentivity of 0.0016 emu/g and saturation magnetization of 0.0097 emu/g) performed via vibrating sample magnetometer suggested its potential applicability in multifunctional devices.*

Keywords: *$Ba(Fe_{1/2}Nb_{1/2})O_3$, green synthesis, structure, dielectric constant, impedance spectroscopy*

I. Introduction

The semiconductor industry's pursuit of ultra-high-density components drives the continual miniaturization of microelectronic devices. Addressing material limitations, researchers are integrating advanced nanomaterials to enhance device performance. Dielectric oxides are vital in microelectronics, with capacitors facing significant miniaturization challenges. Low-dielectric-constant materials are ideal for implementing an insulating layer in integrated circuits, while high-dielectric-constant materials are crucial for applications such as DRAM, energy storage and aerospace technologies. Many high-dielectric-constant materials contain lead, but due to its toxicity there is a demand for sustainable alternatives. Lead-free perovskite $Ba(Fe_{1/2}Nb_{1/2})O_3$ (BFN) ceramics, with dielectric constants around 10^4 [1–5], present a promising solution. The development of nanoscale (<100 nm) BFN ceramic powders is critical for advancing microelectronic compactness and functionality.

Various methods do exist to synthesize oxide nanoparticles, including hydrothermal, solvothermal, ball milling, microemulsion techniques and other chemical routes. However, each of these methods has certain limitations. For instance, they may be energy-intensive, require expensive reagents, involve lengthy processes, or produce toxic by-products. As a result, the development of a cost-effective and green synthesis method for nanomaterials is still a significant challenge. Inorganic molecule interactions with biological systems have emerged as a ground breaking area in

---

[*] Corresponding author: +91 9934837317
e-mail: *prasad_k@tmbuniv.ac.in; k.prasad65@gmail.com*

nanoscience and technology, highlighting the integration of physical, chemical and biological sciences. Recently, green chemistry approaches have been explored for the synthesis of single-phase oxide nanomaterials, offering environmentally sustainable alternatives. Our research group has successfully synthesized various oxide nanomaterials using such approach, targeting different applications [6–13].

Nowadays, the effective recycling and sustainable utilization of domestic waste is a cornerstone of the circular economy. According to the United Nations' 2030 Agenda for Sustainable Development, recovering valuable substances from materials already considered waste is not only advantageous, but also aligns with the principles of green chemistry and circular economy [14]. The nature is intriguing not because of its plethora of organisms but rather due to adaptability of its constituent cohorts. Phyto-diversity is one striking example of it. Different parts of a plant body (such as fruits) divulge a different chemistry during different stages of maturation and ripening. This becomes their chemical identity. Waste citrus fruit like lemon peel, still has many promising metabolites principally citric acid and ascorbic acid along with others. Recently, silver metal and zinc oxide nanoparticles were synthesized using raw orange juice with the idea that the constituent biomolecules will effectively contribute towards the synthesis by their basic chemical properties [15]. The waste lemon peel has identical set of metabolites and/or biomolecules too so we have applied it in order to effectively utilize a common kitchen waste for synthesizing a promising nanomaterial [12,13]. These citrus peels are typically discarded, posing a significant environmental burden [12,13,16].

In this study, a common kitchen waste such as lemon peels was selected to assess its potential for the green synthesis of $Ba(Fe_{1/2}Nb_{1/2})O_3$ nanopowder (abbreviated hereafter as n-BFN). Instead of synthesizing the nanoparticles from individual chemical precursors, the lemon peels were directly employed to challenge microscale $Ba(Fe_{1/2}Nb_{1/2})O_3$. The aim was to develop a green, low-cost and reproducible procedure for the scalable fabrication of n-BFN, with downstream processing in mind which considers the processes involved in separating, purifying and formulating a desired product from a complex biological or chemical mixture. Such nanomaterials could easily be utilized for the fabrication of different nanocomposites and/or ceramics after sintering for various industrial applications. The synthesized n-BFN were extensively characterized using X-ray diffraction, transmission electron microscopy, scanning electron microscopy, energy dispersive spectroscopy, complex impedance spectroscopy and vibrating sample magnetometer techniques. Additionally, an investigation was conducted to elucidate the potential mechanisms underlying the green synthesis and transformation from micro- to nano-scale product by the waste lemon peels.

II. Experimental

$Ba(Fe_{1/2}Nb_{1/2})O_3$ ceramic powder was synthesized by conventional mixed oxide method using high-purity AR grade (purity > 99.9%) Merck chemicals: $BaCO_3$, Fe_2O_3 and Nb_2O_5. The thermochemical reaction was carried out at 1200 °C/5 h and the formation of the appropriate $Ba(Fe_{1/2}Nb_{1/2})O_3$ phase was confirmed by X-ray diffraction method. The obtained sample is abbreviated as BFN.

The sample abbreviated as n-BFN was synthesized by using 50 g of fresh lemon peels waste. The lemon peels were thoroughly cleaned with distilled water and then homogenized in a mixer grinder to form a slurry. The slurry was then mixed with 200 ml of 70% methyl alcohol in an Erlenmeyer flask and heated in a steam bath at 80 °C for 30 min with occasional stirring to extract metabolites such as organic acids, polyphenols and terpenoids. Then the solution was allowed to cool to ambient temperature and subsequently filtered using a Büchner funnel. The resulting filtrate (approximately 150 ml) was transferred to another Erlenmeyer flask and its volume was reduced by further heating at 80 °C for 20 min in a steam bath (the pH of the solution was between 6.5 and 8). Subsequently, 50 ml of the previously prepared aqueous $Ba(Fe_{1/2}Nb_{1/2})O_3$ slurry was introduced into the waste lemon extract. The pH of the control solution was measured and found to be within the range of 5.5 to 7.5. The reaction solution was further processed, i.e. the mixture was maintained at 80 °C for an additional 30–45 min, during which a faint brownish haze appeared. This was accompanied by the formation of a light brown precipitate at the base of the flask, implying the initiation of the transformation to nano-scale product. This process was continued to complete the transformation process and the flask was subsequently incubated at room temperature for 9 h, leading to the formation of distinct brown clusters at the base of the flask. A marginal drop in pH to 6 was observed in the reaction solution, while the control remained at 6.5.

The dried $Ba(Fe_{1/2}Nb_{1/2})O_3$ powders were compacted into circular disc-shaped pellets with a thickness of 1.6 mm and a diameter of 9.5 mm using uniaxial pressure of approximately 650 MPa. The resulting pellets were subsequently sintered at 1225 °C/4 h to achieve densification. The density of sintered pellet was determined using its geometrical measurements and water immersion (Archimedes) technique. The density of the obtained ceramics was found to be ~93% of the theoretical one.

The X-ray diffraction (XRD) patterns of the BFN and n-BFN powders were obtained at ambient temperature utilizing an XPERT PRO (PW-35/60) diffractometer with CuKα radiation (λ = 1.5406 Å). Data acquisition was performed over the angular range $20° \leq 2\theta \leq 80°$ at a scanning rate of 2 °/min. The crystal structure and lattice parameters were refined using the Rietveld method implemented in FullProf 2000 software. Morphological and particle size characterization of the n-BFN powder was carried out via scanning electron microscopy (SEM) and transmission electron microscopy (TEM). SEM images were recorded using a JEOL-JSM840A microscope, and high-resolution TEM (HRTEM) images were captured with a Bruker TEM operating at 200 keV. The sample for TEM analysis was prepared by suspending the n-BFN particles in distilled water, followed by ultrasonic dispersion to isolate individual particles. The magnetic characteristics of the n-BFN were investigated at ambient temperature using a vibrating sample magnetometer (VSM, model PAR-155). The dielectric and impedance spectroscopies were performed as a function of frequency (20 Hz to 10 MHz) and temperature (20 to 500 °C) simultaneously using an Agilent 4294A impedance analyser with a computer-controlled setup. A symmetric Ag|n-BFN|Ag cell configuration was employed, where silver (Ag) conductive paint was applied to both surfaces of the sintered n-BFN pellet. The temperature during the cooling phase was incrementally reduced at 1 °C/min to monitor the temperature-dependent impedance response.

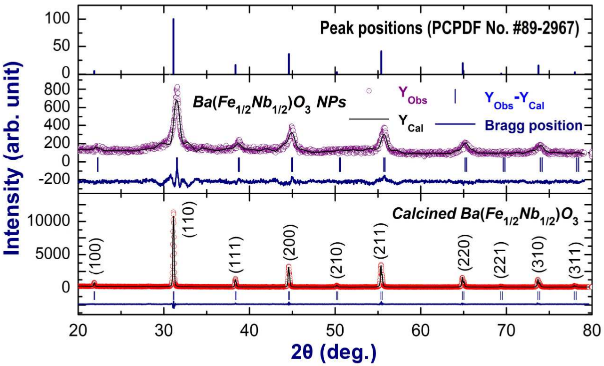

Figure 1. Rietveld refined XRD patterns of calcined BFT powder (lower) and n-BFT nanoparticles (middle) at room temperature – peak positions as per PCPDF No. #89-2967 are also shown

III. Results and discussion

Figure 1 depicts the Rietveld refined XRD patterns of the BFN and n-BFN powders along with the peak positions. The Rietveld refinement of XRD patterns confirmed that both samples possessed a cubic unit cell with space group: $Pm\bar{3}m$ (221) in Hermann-Mauguin notation, aligning closely with the reported reference value (JCPDS-ICDD file No. #89-2967). The lattice parameters derived via least-squares regression were a = 4.0597 Å for the BFN powder and a = 4.0563 Å for the n-BFN sample prepared using waste lemon peel extract. The indexing reliability ($\chi^2 \approx 1.9$) was assessed by minimizing the deviation $\sum(d_{obs} - d_{calc})$. For the n-BFN powder, peak broadening and reduced intensities in the XRD profiles were observed, implying either a nanoscale crystallite size or partial amorphousness. Additionally, a little shift of XRD peaks to higher 2θ values is observed in Fig. 1, pointing to a very small unit cell contraction. Difference in the lattice parameter of 0.0034 Å was calculated between the BFN and n-BFN samples. This difference causes a slight reduction in unit cell volume from 66.9086 Å^3 (BFN) to 66.7406 Å^3 (n-BFN) attributed to the size-induced lattice effects. This result is in consistent with the earlier report [11].

Figures 2a,b display SEM and TEM images of the synthesized n-BFN powder. Both micrographs clearly reveal the presence of individual nanoparticles along with a very few aggregates. The particle size histogram (Fig. 2a, inset) shows a distribution of particle sizes which ranged from 11–48 nm. This size variation is attributed to the sequential formation of nanoparticles at different stages during the synthesis process.

In order to confirm the absence of the second phase after sintering, energy dispersive spectroscopy (EDS) was carried. Figure 3 illustrate the EDS pattern and SEM micrograph of the sintered n-BFN ceramics. All the peaks in the pattern were perfectly assigned to the elements present in Ba(Fe$_{1/2}$Nb$_{1/2}$)O$_3$ (Table 1). This clearly indicated the purity and formation of the n-BFN

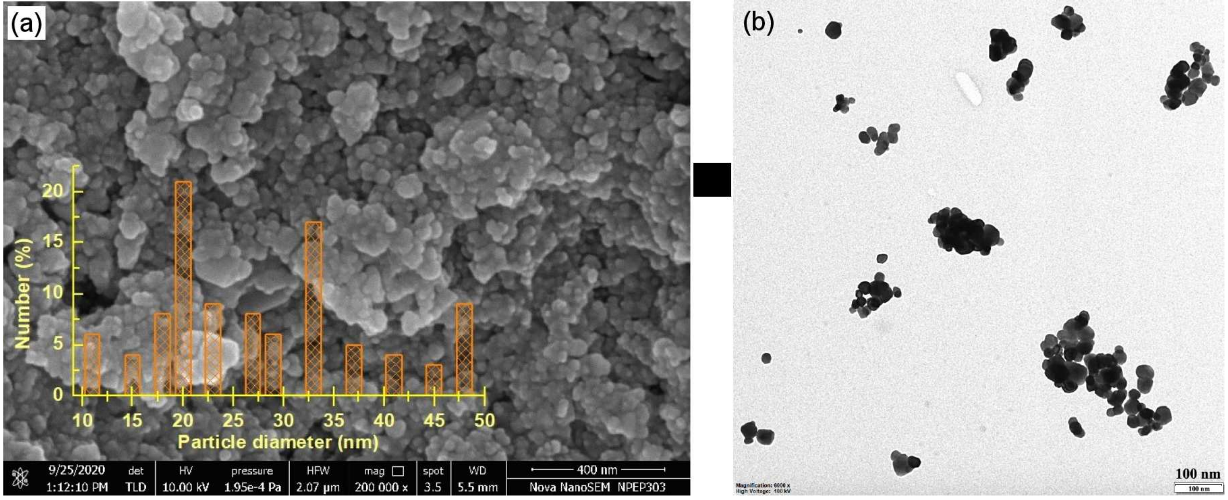

Figure 2. SEM image with particle size distribution as inset (a) and TEM image of as-synthesized Ba(Fe$_{1/2}$Nb$_{1/2}$)O$_3$ nanopowder using waste lemon peel extract (b)

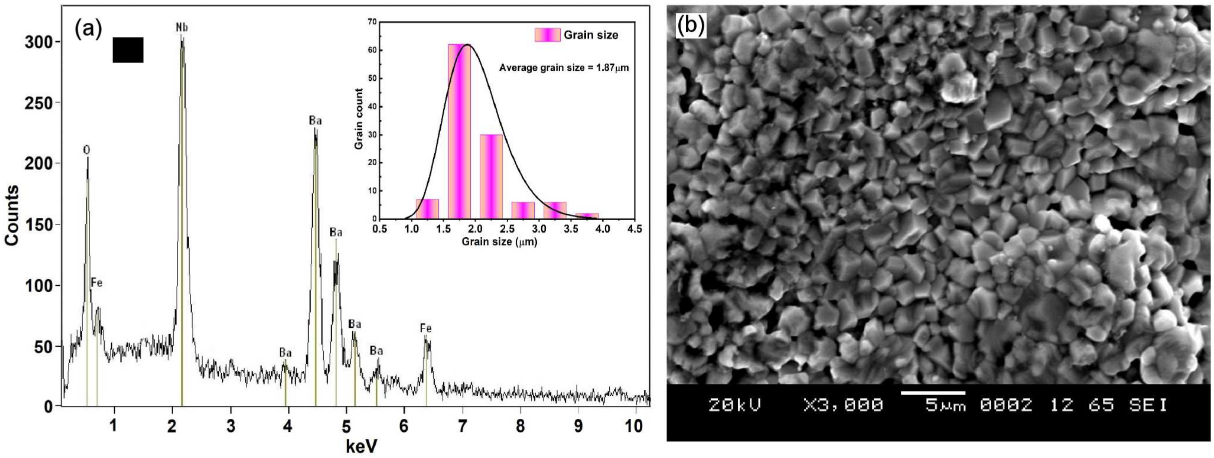

Figure 3. EDS with grain size distribution shown in inset (a) and SEM micrograph (b) of the sintered n-BFN ceramics

Table 1. Quantitative results of EDS for Ba($Fe_{1/2}Nb_{1/2}$)O_3 nanoceramic powder

Element / line	Net counts	Content [wt.%]	Content [at.%]
O *K*	1115 ± 62	8.02 ± 0.45	36.94 ± 2.05
Fe *K*	832 ± 88	10.36 ± 1.10	13.66 ± 1.44
Nb *L*	4983 ± 164	21.87 ± 0.72	17.34 ± 0.57
Ba *L*	5940 ± 190	59.75 ± 1.91	32.05 ± 1.03
Total		100.00	100.00

ceramics. Grain structure is clearly visible in SEM micrograph of the sintered n-BFN sample, indicating the existence of polycrystalline microstructure. The grains of unequal sizes (1.25–3.75 μm) appear to be distributed throughout the sample. The analysis of grain size distribution was estimated using *ImageJ* software which clearly indicated the average grain size to be 1.87 μm (inset in Fig. 3a).

Figure 4 illustrates the schematics of the process adopted for the green synthesis of the n-BFN using wasted lemon peel. It is known that the lemon peel extract is rich in bioactive natural compounds, such as prenyloxycoumarins (e.g. bergamottin, auraptene, heraclenin, inva-torin, oxypeucesanin) [17–21], essential oils (e.g. geranyl acetate, limonene, citronellal, linalyl, α-terpineol) [22–25] and citric acid as well as ascorbic acid [26].

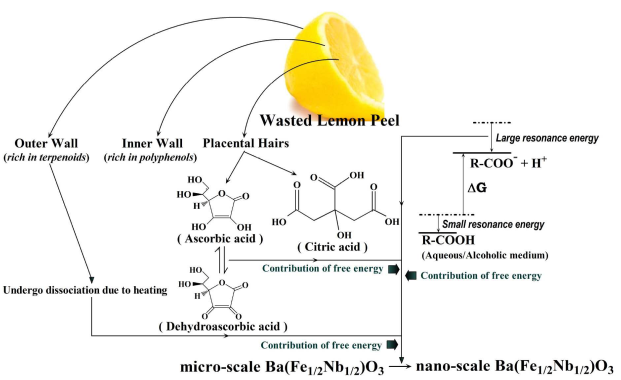

Figure 4. Schematics for the green synthesis of BFN nanopowders using waste lemon peel

The nucleation and growth theory for the formation of spherical particles is expressed as [12,13]:

$$\Delta G = -\frac{4}{V}\pi r^3 k_B T \ln(S) + 4\pi r^2 \gamma \tag{1}$$

where V, r, S and γ are the molecular volume, nucleus radius, saturation ratio and free energy per unit surface area. According to this theory, the synthesis process requires overcoming the overall free energy change (ΔG), a combination of the energy associated with new volume formation and the energy of the newly created surface area, i.e. decrease in γ or increase in S leads the transformation of the micro-scale BFN to nano-scale BFN. It is also known that under the oxidizing conditions, ascorbic acid converts into dehydroascorbic acid, while citric acid and citrate ions release free energy ($\Delta G \sim 47$ kJ/mol) via resonance stabilization, promoting the transformation of BFN to n-BFN [26]. Additionally, the breakdown of pectins, terpenes and flavonoids further supports the synthesis mechanism. These compounds, obeying the principles of chemistry under the change of medium conditions, contribute to the process by reducing γ and enhancing S, with citric acid, ascorbic acid and their derivatives playing a crucial role in the synthesis of n-BFN. This process exemplifies a green chemistry approach, leveraging domestic waste (e.g. waste lemon peels) for material synthesis, aligning with circular economy principles. Compared to conventional methods, it is cost-effective, reproducible, non-toxic and environmentally friendly. Previously, similar strategies enabled the synthesis of Ag and ZnO nanoparticles using orange juice [15]. Here, waste lemon peels are innovatively utilized to produce n-BFN, demonstrating an efficient and sustainable alternative to traditional

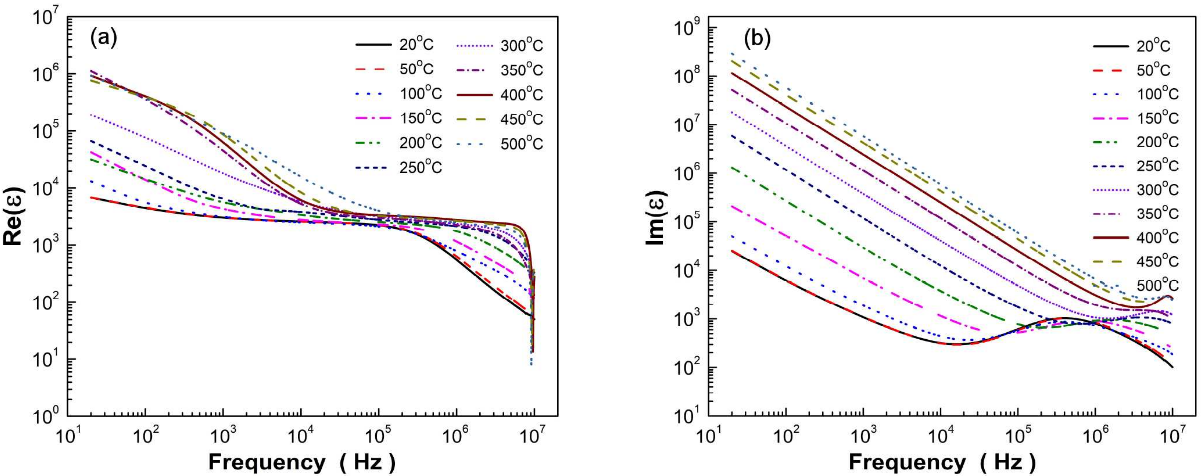

Figure 5. Variation of real (a) and imaginary (b) parts of dielectric constant with frequency at different temperatures for sintered n-Ba($Fe_{1/2}Nb_{1/2}$)O_3 ceramics

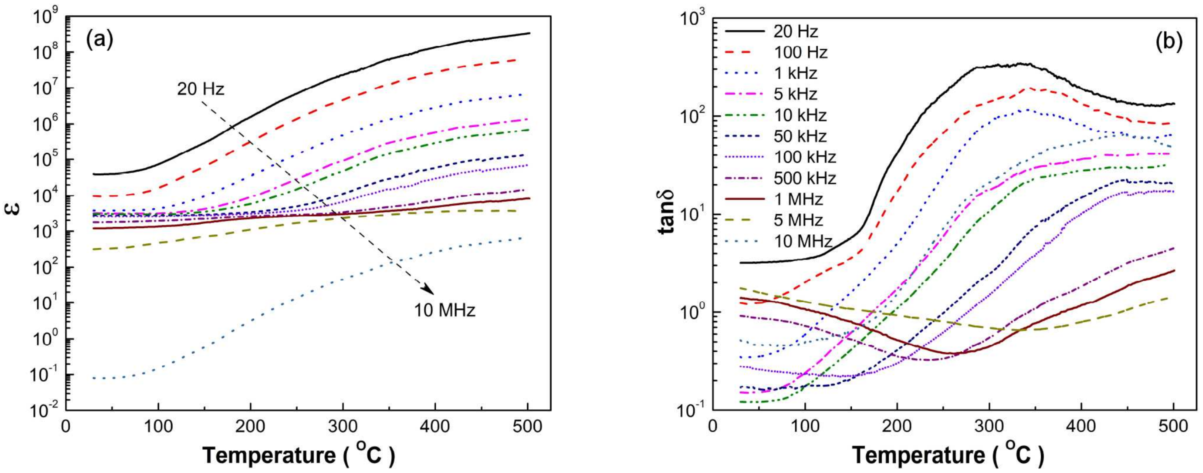

Figure 6. Variation of dielectric constant (a) and tangent loss (b) with temperature at different frequencies for sintered n-Ba($Fe_{1/2}Nb_{1/2}$)O_3 ceramics

synthesis techniques.

Figure 5 illustrates the frequency-dependent behaviour of the real part (ε') and imaginary (ε'') part of the dielectric constant of the sintered n-BFN samples at various temperatures. Both ε' and ε''’ exhibit a decreasing trend with increasing frequency. Such behaviour is related to the polarization mechanism [27–29]. In the ε''–f plots, a broad peak is observed at all temperatures, with the peak shifting to higher frequencies as the temperature rises. The ε'–f curves show significant dispersion at lower frequencies, where the dielectric constant is relatively high, followed by a gradual decrease at higher frequencies. This elevated dielectric constant at low frequencies can be attributed to the space charge polarization. At very low frequencies, the dipoles align effectively with the applied field, resulting in ε' approaching ε_∞, the static dielectric constant. As the frequency increases, the dipoles lag behind the field, causing a gradual reduction in ε'. Beyond a characteristic frequency, a sharp decline in ε' is observed, signifying a relaxation process. At very high frequencies, dipoles fail to respond to the rapidly oscillating field, and ε' approaches ε_∞, the dielectric constant at infinite frequency.

Temperature-dependent variations of dielectric constant (ε) and tangent loss ($\tan\delta$) for the sintered n-BFN samples at different frequencies are shown in Fig. 6. The values of ε increase with rising temperature across all frequencies. Similarly, $\tan\delta$ also increases, reaching a peak that shifts to higher temperatures as frequency increases. Additionally, *tanδ* initially decreases but then begins to rise beyond 500 kHz. At 20 °C, ε' and ε'' values are 104466 and 36589, respectively, at a frequency of 1 kHz. The high dielectric constant (~10^4) and loss tangent ($\tan\delta = \varepsilon''/\varepsilon'$) of 0.35 at room temperature indicate the potential suitability of the n-BFN ceramics for diverse electronics, aerospace and industrial applications.

The variation of the real (Z') and imaginary (Z'') components of impedance with frequency for the n-BFN ceramics at various temperatures is presented in Fig. 7. A noticeable trend is that Z' decreases progressively as the frequency increases, regardless of the temperature. In contrast, Z''–f plots (loss spectrum) ex-

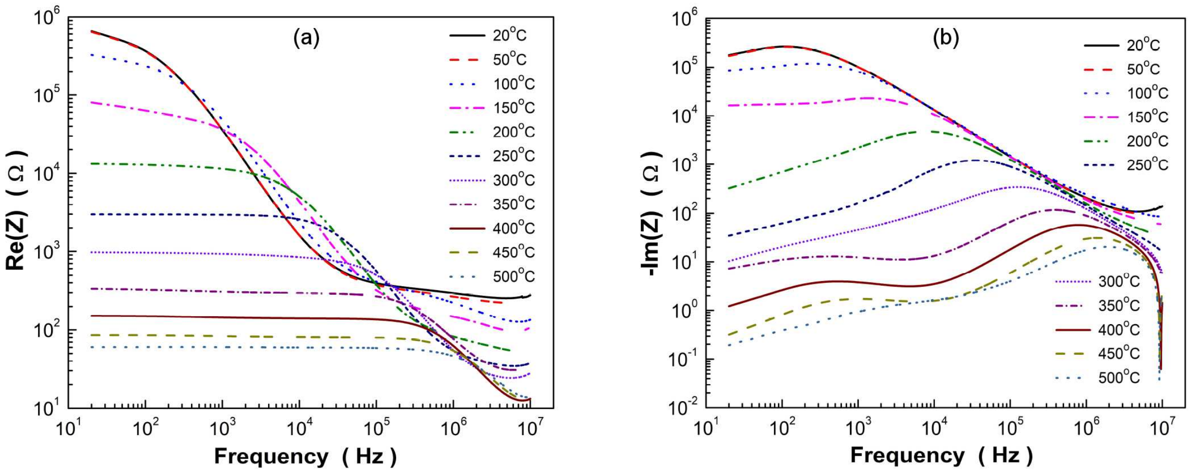

Figure 7. Variation of real (a) and imaginary (b) parts of impedance with frequency at different temperatures for sintered n-Ba($Fe_{1/2}Nb_{1/2}$)O_3 ceramics

hibit notable features, including the appearance of peaks (Z''_{max}), which are slightly asymmetric. The Z''_{max} values display a decreasing trend and shift toward higher frequencies as the temperature increases, as observed in the $Z''-f$ plots. The broadening of peaks, asymmetric in nature, suggests a distribution of relaxation times, indicative of temperature-dependent electrical relaxation within the material [30].

The complex impedance spectra of the n-BFN ceramics in the investigated frequency range at various temperatures are illustrated in Fig. 8. The impedance curves progressively bend toward the x-axis upon incrementing the temperature, reflecting enhanced electrical conductivity in the specimen. Furthermore, the complex plane plots form depressed semicircular arcs that are asymmetric, which shift toward higher Z' values as temperature increases. This behaviour points to significant contributions from grain boundary effects, as highlighted in the insets of Fig. 8. In such a situation the data cannot be well approximated by the impedance and capacitance only. It can be seen that a constant phase element (Q) and Warburg element (W) along with the resistances and capacitances are connected throughout the temperature range of measurement. The appropriate equivalent circuits at three representative temperatures are illustrated in the insets of Fig. 8. The parameters of each fitting are summarized in Table 2 along with the χ^2-values which were determined using a non-linear least-square fitting algorithm [31]. The introduction of Q in the equivalent circuit may be due to the distribution of reaction rates and/or surface roughness whereas the W may be due to the semi-infinite linear diffusion, i.e. unrestricted diffusion to a large planar electrode, which obeys the second Fick's law. Also, all these curves do not coincide with origin (zero value) and hence a series resistance has been introduced that can be ascribed to the LCR circuit representation of the sample. The impedance data did not fit well with the single RC-combination, but it fits excellently well with equivalent circuits shown in insets of Fig. 8, indicating thereby that the electrical responses are due to the grain and grain boundary effects. It is observed that all the circuit models fitted excellently well ($\chi^2 \sim 10^{-3}$) with the experimental data (Table 2). Usually, for an ideal Debye type relaxation, semicircular impedance plots with centres on the Z'-axis are expected. However, the Argand plane plots reveal depressed semicircles with centres below the Z'-axis, characteristic of non-Debye-type relaxation. This behaviour can be described by the following equation:

$$Z^*(\omega) = Z' + iZ'' = \frac{R}{1 + \left(\frac{i\omega}{\omega_0}\right)^{1-\alpha}} \tag{2}$$

where α quantifies the deviation from ideality. For $\alpha = 0$, the equation reduces to the classical Debye model. The observed depressed arcs confirm $\alpha > 0$, with α increasing as the temperature rises, further supporting non-Debye type relaxation in the material. This phenomenon aligns with earlier reports [32–35], likely stemming from distributed elements within the

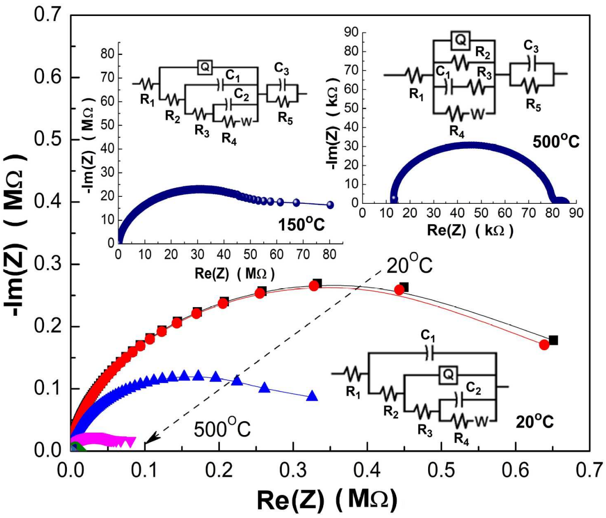

Figure 8. Complex impedance plots of n-BFN ceramics at different temperatures (insets show enlarged view for two temperatures and appropriate equivalent electrical circuits)

Table 2. Calculated parameters of each fit corresponding to the equivalent circuits shown in Fig. 8

Parameters	Temperature		
	20 °C	150 °C	500 °C
R_1 [Ωcm^2]	0.01749	21.3	0.0002278
R_2 [Ωcm^2]	236.4	5.273×10^4	86.39
R_3 [Ωcm^2]	3.469×10^5	2.593×10^4	17.47
R_4 [Ωcm^2]	1.573×10^5	8.702×10^5	893.2
R_5 [Ωcm^2]	-	90.61	0.002045
C_1 [F/cm^2]	3.338×10^{-11}	3.744×10^{-8}	1.434×10^{-9}
C_2 [F/cm^2]	5.766×10^{-9}	6.241×10^{-7}	1.298×10^{-20}
C_3 [F/cm^2]	-	1.154×10^{-10}	-
CPE (Q), Y_0 [S s$^{0.5}$/cm^2]	2.818×10^{-9}	3.756×10^{-9}	1.9×10^{-16}
Frequency power, n	0.9428	0.9065	0.3732
Warburg, W [S s$^{0.5}$/cm^2]	1.323×10^{-6}	0.0001091	1.015×10^{-5}
χ^2	1.853×10^{-3}	2.553×10^{-3}	4.936×10^{-3}

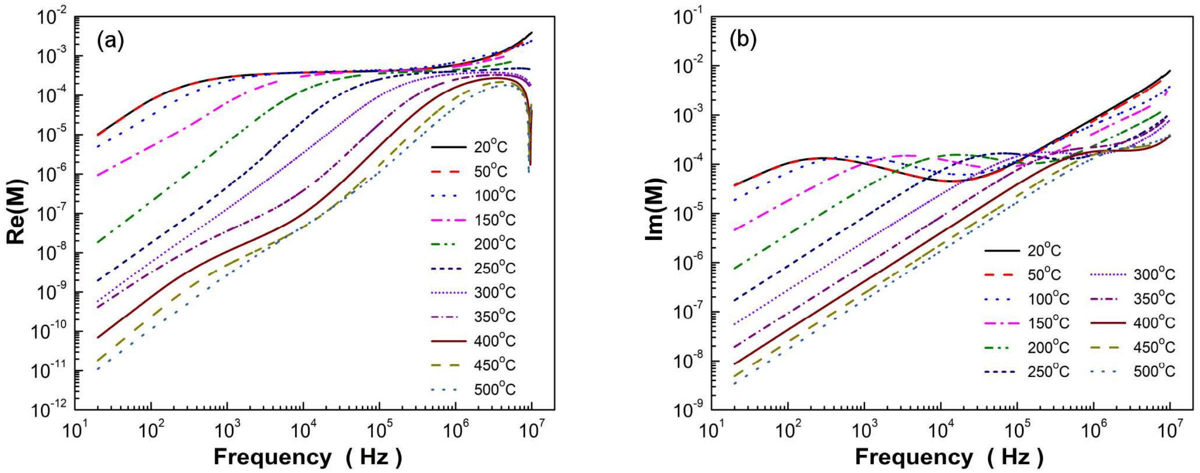

Figure 9. Variation of real (a) and imaginary (b) parts of electric modulus with frequency at different temperatures for sintered n-Ba(Fe$_{1/2}$Nb$_{1/2}$)O$_3$ ceramics

material-electrode system. These elements, attributed to the microstructural inhomogeneities such as grain boundaries or defects, disrupt ideal Debye behaviour and influence relaxation dynamics.

The electric modulus, defined as the reciprocal of the dielectric response, $M^*(\omega) = 1/\varepsilon^*(\omega)$, mitigates electrode polarization effects. M^* is characterized by a sigmoidal step in the real part (M') and a broad, asymmetric peak in the imaginary part (M''), reminiscent of mechanical relaxation processes. Figure 9 illustrates the frequency dependence of M' and M'' across temperatures for the sintered n-BFN ceramics. At low frequencies, M' is minimal but exhibits a sigmoidal rise, converging to M_∞ at higher frequencies, indicative of short-range charge carrier mobility [32]. M'' reveals distinct features, including temperature-specific peaks, asymmetry and a shift to higher frequencies with increasing temperature. These peaks signify transitions from long-range to localized charge motion and indicate conductivity relaxation. The observed broadening of M'' with temperature implies enhanced non-Debye behaviour, contrasting with the trend seen in mechanical or optical relaxation phenomena [33].

Figure 10a presents the AC electrical conductivity (σ_{AC}) of the n-BFN ceramics as a function of frequency at various temperatures. The data reveal frequency-dependent dispersion, transitioning to a plateau at elevated temperatures. This shift marks the onset of conductivity relaxation, highlighting a transition from the long-range hopping to the localized ionic motion. The observed hopping mechanism aligns with a high density of states in materials with semiconductor-like band gaps, where charge carrier localization promotes polaron formation and the nearest-neighbour hopping conduction [2,36]. The temperature-dependent plots of σ_{AC} at different frequencies are presented in Fig. 10b. The Arrhenius relationship was used to estimate the apparent activation energy (E_a):

$$\sigma_{AC} = \sigma_0 + \exp\left(-\frac{E_a}{k_B T}\right) \tag{3}$$

where k_B is the Boltzmann constant, T is the absolute temperature and σ_0 is the pre-exponential factor.

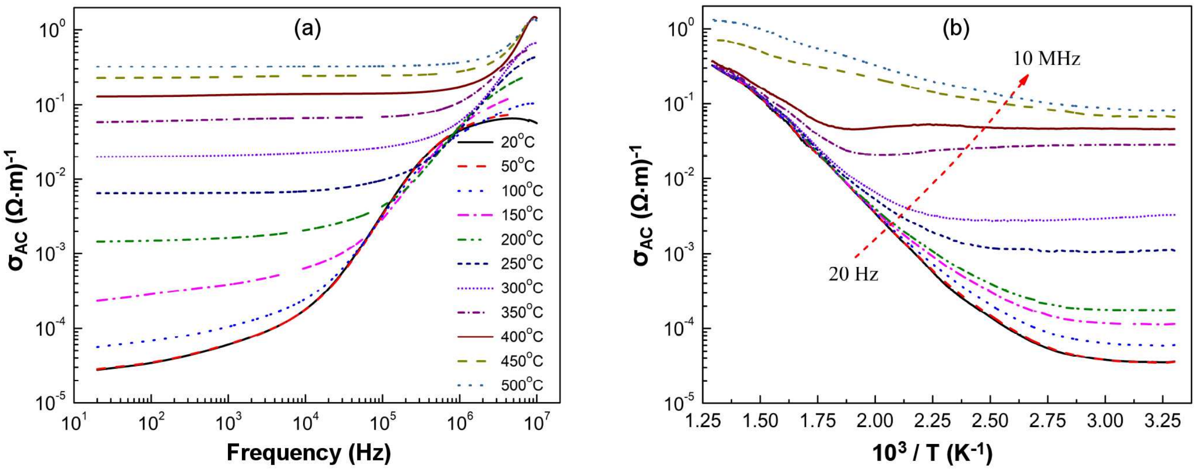

Figure 10. Variation of AC conductivity with: a) frequency at different temperatures and b) temperature at different frequencies for sintered n-Ba($Fe_{1/2}Nb_{1/2}$)O_3 ceramics

By applying linear least squares fitting to the experimental data of the high-temperature region, the values of E_a were determined to be approximately 0.47 eV at 1 kHz and 0.21 eV at 1 MHz. Relatively low values of E_a suggest that the carrier transport predominantly occurs through hopping mechanisms between localized states, indicative of a disordered structure [37,38]. The high conductivity observed in the n-BFN ceramics is attributed to the oxygen vacancies introduced during the sintering process:

$$O_O \longrightarrow \frac{1}{2}O_2\uparrow + V_O^{\bullet\bullet} + 2e^- \tag{4}$$

where $V_O^{\bullet\bullet}$ represents the doubly ionized oxygen vacancies. These vacancies enhance conductivity by facilitating charge transport, albeit at the expense of increased dielectric loss and space charge accumulation at grain boundaries, which may degrade the overall performance of the material [39]. Further, σ_{AC} for materials with localized states can be described by the Jonscher power law [30,34]:

$$\sigma_{AC} = \sigma_0 + A\omega^s \tag{5}$$

where σ_0 is the frequency-independent direct current component, A is a temperature-dependent constant, $\omega = 2\pi f$ is the angular frequency and s ($0 \le s \le 1$) is an exponent that reflects the conduction mechanism. The constant A can be expressed as:

$$A = \frac{\pi N^2 e^2}{6k_B T(2\alpha)} \tag{6}$$

where e is the electronic charge, α is the polarizability of the site pair and N is the number of sites per unit volume available for hopping. In this context, σ_{AC} arises from the carrier displacement through discrete hopping between localized states. The term $A\omega^s$ is consistent with two primary conduction models:

i. Quantum mechanical tunneling (QMT) - carriers tunnel through barriers separating localized sites, leading to a temperature-independent s that decreases with increasing ω.
ii. Correlated barrier hopping (CBH) - carriers hop over potential barriers, with σ_{AC} expressed as [31,40]:

$$\sigma_{AC} = \frac{\pi}{3}e^2\omega k_B T\left[N(E_f)\right]^2\alpha^{-5}\left[\ln\frac{f_0}{\omega}\right]^4 \tag{7}$$

where $N(E_f)$ is the density of states at the Fermi level.

The exponent s and minimal hopping distance R_{min} are given by [41]:

$$s = 1 - \frac{6k_B T}{W_m} \tag{8}$$

$$R_{min} = \frac{2e^2}{\pi\varepsilon\,\varepsilon_0 W_m} \tag{9}$$

where W_m is the binding energy, representing the energy required to completely transfer an electron between sites and ε_0 is the dielectric constant of vacuum. The experimental results reveal that s exhibits contrasting trends depending on the conduction mechanism. In QMT, s remains constant with temperature but decreases with frequency, whereas in CBH, s varies with both temperature and frequency. The hopping conduction model indicates a significant role of localized states and barrier interactions in determining σ_{AC}. Estimations of $N(E_f)$ using $f_0 = 10^{13}$ Hz and $\alpha = 10^{10}\,m^{-1}$ further validate the proposed mechanisms across different temperatures and frequencies.

Figure 11a presents the frequency dependent variation of $N(E_f)$ at various temperatures. The data indicate a reduction in $N(E_f)$ with increasing frequency, converging at frequencies exceeding 100 kHz. The inset in Fig. 11a illustrates the variation of $N(E_f)$ with temperature across different frequencies for the n-BFN ceramics. An increase in $N(E_f)$ is observed with rising temperature for all frequencies investigated. At lower

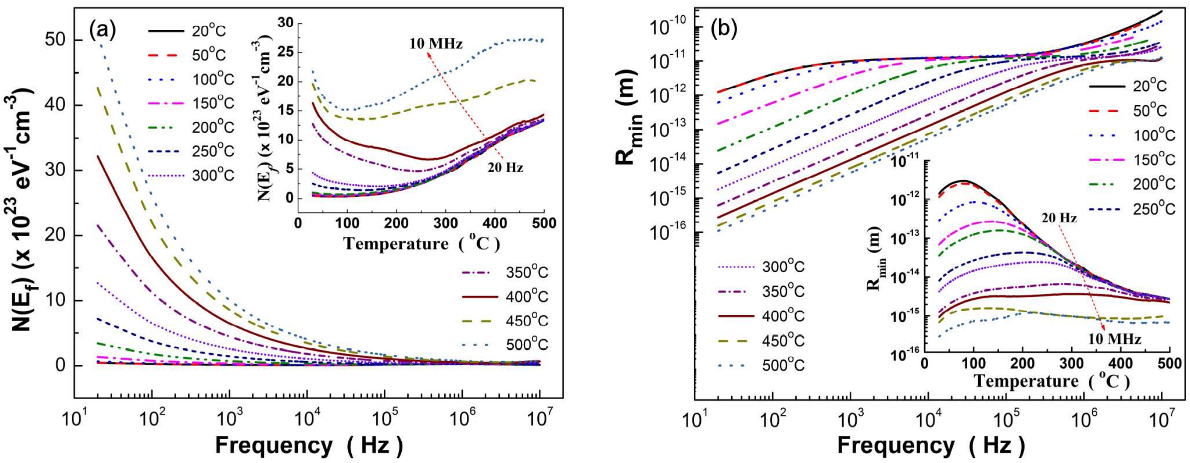

Figure 11. Variation of $N(E_f)$ with frequency at different temperatures (a) and variation of R_{min} with frequency at different temperatures (b) for sintered n-Ba(Fe$_{1/2}$Nb$_{1/2}$)O$_3$ ceramics

frequencies, the electrical conduction in the system is influenced by both frequency and temperature. Conversely, at higher frequencies, charge carriers become localized, and their behaviour is predominantly governed by thermal excitations. This frequency-dependent response aligns with the results from AC conductivity measurements depicted in Fig. 10b. Relatively high values of $N(E_f)$ suggest that charge transport in the n-BFN ceramics is primarily facilitated through the hopping mechanism between localized states. These observations are consistent with previous reports [2,42].

Figure 11b illustrates the frequency dependence of R_{min} at various temperatures. In the low-frequency region, R_{min} exhibits a small value (~ 10^{-11} m), followed by continuous dispersion with increasing frequency and a tendency to saturate at a maximum asymptotic value in the high-frequency region. This behaviour can be attributed to the absence of a restoring force that governs charge carrier mobility under the influence of an induced electric field, facilitating long-range charge carrier mobility. Furthermore, the sigmoidal increase in R_{min} with frequency, eventually approaching a saturation value, is indicative of a conduction mechanism dominated by short-range charge carrier mobility at higher frequencies [42]. Besides, the variation of R_{min} with temperature at different frequencies (Fig. 11b, inset), reveals a decrease in R_{min} with rising temperature at lower frequencies. This trend reaches a maximum, consistent with earlier observations. Notably, R_{min} was approximately 10^4 times smaller than the grain size of the n-BFN ceramics, underscoring the localized nature of the conduction mechanism.

Figure 12 illustrates the dependence of magnetization (M) on the applied magnetic field (H) for both the BFN and n-BFN powders at room temperature. The M-H curve for the BFN sample exhibits a well-saturated weak ferromagnetic hysteresis, whereas the curve for the n-BFN is narrower and does not achieve complete saturation until an applied field of 10 kOe is reached. This behaviour reflects the influence of nanoscale effects, implying that the particles in the n-BFN powder are extremely small. It is seen that the BFN powder exhibits a coercive field (H_c) of 319.5 Oe, a retentivity (M_R) of 0.0042 emu/g, and a saturation magnetization (M_S) of 0.0129 emu/g which compares well with the earlier report [4]. In comparison, these values for the n-BFN sample are significantly reduced to 126 Oe, 0.0016 emu/g, and 0.0097 emu/g. The observed decrease in H_c and M_R for the n-BFN powder may be attributed to the reduced number of coupling between iron ions, leading to a lower coercive field and minimal retentivity. Similarly, M_S is also observed to be lower in the n-BFN sample. The reduced H_c in the n-BFN suggests potential utility in recording applications due to its favourable low-field response.

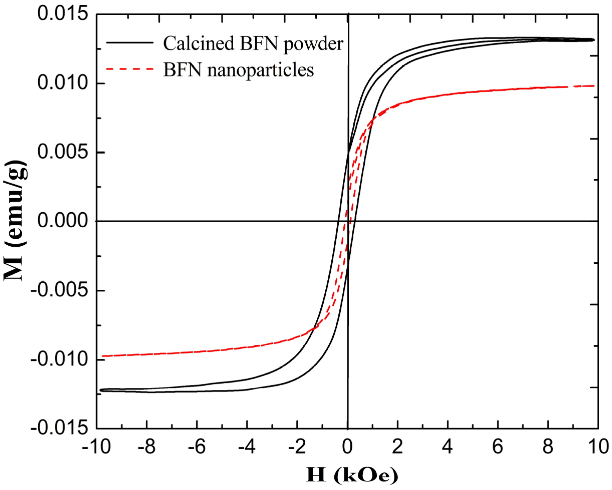

Figure 12. Magnetization curve of microscale and nanoscale Ba(Fe$_{1/2}$Nb$_{1/2}$)O$_3$ powders at room temperature

IV. Conclusions

The synthesis process using waste lemon peels described herein represents an environmentally friendly and cost-efficient strategy for synthesizing promising dielectric nanoceramic powder of Ba(Fe$_{1/2}$Nb$_{1/2}$)O$_3$ (n-

BFN). This approach not only streamlines the production of advanced ternary and higher-order oxide systems, but also addresses critical challenges related to achieving precise stoichiometry. XRD analyses confirmed the formation of a single-phase BFN with cubic structure (a = 4.0597 Å; space group: $Pm\bar{3}m$). TEM and SEM images revealed both individual nanoparticles and a few aggregates whose sizes varied between 11 and 48 nm. Synthesis of the n-BFN is likely driven by the redox interconversion of ascorbic acid and the resonance energy contributions from citric acid and citrate ions. The complex impedance and electric modulus spectroscopy studies indicated the dielectric relaxation behaviour of the sintered n-BFN to be of non-Debye type. The correlated barrier hopping model favourably explains the mechanism of charge transport within the material. Exhibiting a high dielectric constant ($\sim 10^4$) and a low loss tangent (0.35) at room temperature, the n-BFN ceramics demonstrates significant promise for diverse electronic and industrial applications. Additionally, magnetic characterization (coercive field of 126 Oe, retentivity of 0.0016 emu/g and saturation magnetization of 0.0097 emu/g) suggests the potential of the n-BFN to be used in different multifunctional devices.

Acknowledgments: The authors express their sincere gratitude to the Central Instrumentation Facility at Savitribai Phule Pune University, Pune, India, for their generous support in providing XRD data, and SEM as well as TEM images.

References

1. I.M. Reaney, J. Petzelt, V.V. Voitsekhovskii, F. Chu, N. Setter, "B-Site Order and infrared reflectivity in A(B'B")O$_3$ complex perovskite ceramics", *J. Appl. Phys.*, **76** (1994) 2086–2092.
2. S. Bhagat, K. Prasad, "Structural and impedance spectroscopy analysis of Ba(Fe$_{1/2}$Nb$_{1/2}$)O$_3$ ceramic", *Phys. Status Solidi A*, **207** (2010) 1232–1239.
3. R. Köferstein, F. Oehler, S.G. Ebbinghaus, "Magnetic, optical, dielectric, and sintering properties of nanocrystalline BaFe$_{0.5}$Nb$_{0.5}$O$_3$ synthesized by a polymerization method", *J. Mater. Sci.*, **53** (2017) 1024–1034.
4. H. Ranjan, U.K. Mahto, K.P. Chandra, A.R. Kulkarni, A. Prasad, K. Prasad, "Electrical and magnetic properties of 0-3 Ba(Fe$_{1/2}$Nb$_{1/2}$)O$_3$/PVDF composites", *J. Adv. Dielectr.*, **7** (2017) 1750036.
5. D. Bochenek, P. Niemiec, M. Adamczyk, I. Szafraniak-Wiza, "Physical properties of lead-free BaFe$_{1/2}$Nb$_{1/2}$O$_3$ ceramics obtained from mechanochemically synthesized powders", *J. Mater. Sci*., **53** (2018) 13501–13512.
6. A.K. Jha, K. Prasad, K. Prasad, "Biosynthesis of Sb$_2$O$_3$ nanoparticles: A low cost green approach", *Biotechnol. J.*, **4** (2009) 1582–1585.
7. A.K. Jha, K. Prasad, K. Prasad, "A green low-cost biosynthesis of Sb$_2$O$_3$ nanoparticles", *Biochem. Eng. J.*, **43** (2009) 303–306.
8. A.K. Jha, K. Prasad, "Ferroelectric BaTiO$_3$ nanoparticles: biosynthesis and characterization", *Coll. Surf. B Biointerf.*, **75** (2010) 330–334.
9. A.K. Jha, K. Prasad, "Biosynthesis of metal and oxide nanoparticles using *Lactobacilli* from yoghurt and probiotic spore tablets", *Biotechnol. J.*, **5** (2010) 285–291.
10. A.K. Jha, K. Prasad, "Carbon coated alumina nanoparticles: A green option for water purification", *J. Bionanosci.*, **6** (2012) 33–38.
11. A.K. Jha, K. Prasad, "Green synthesis and characterization of BaFe$_{0.5}$Nb$_{0.5}$O$_3$ nanoparticles", *J. Chin. Adv. Mater. Soc.*, **2** (2014) 294–302.
12. R. Prasad, A.K. Jha, K. Prasad, *Exploring the Realms of Nature for Nanosynthesis*, Springer Int. Publ. Switzerland, 2018.
13. K. Prasad, G.P. Singh, A.K. Jha, *Nanofabrication Enrapturing Cues and Prodigal Applications*, CRC Press, USA, 2024.
14. https://www.un.org/sustainabledevelopment/sustainable-development-goals/
15. A.K. Jha, V. Kumar, K. Prasad, "Biosynthesis of metal and oxide nanoparticles using orange juice", *J. Bionanosci*., **5** (2011) 162–166.
16. B. Nayak, F. Dahmoune, K. Moussi, H. Remini, S. Dairi, O. Aoun, M. Khodir, "Comparison of microwave, ultrasound and accelerated-assisted solvent extraction for recovery of polyphenols from Citrus sinensis peels", *Food Chem.*, **187** (2015) 507–516.
17. I.B. Chatterjee, C.K. Mukhopadhyay, M.K. Ghosh, "Vitamin C: A potential saviour against free radical-induced oxidative damage", *Curr. Sci.*, **69** (1995) 747–751.
18. Y. Miyake, K. Yamamoto, Y. Morimitsu, T. Osawa, "Isolation of *C*-Glucosylflavone from lemon peel and antioxidative activity of flavonoid compounds in lemon fruit", *J. Agri. Food Chem.*, **45** (1997) 4619–4623.
19. N.Y.T. Tran, N.P.T. Nhan, V.T. Thanh, D.V. Nguyen, P.V. Thinh, T.A. Vy, T.D. Lam, T.T. Truc, "Effects of drying conditions on total phenolic content and other parameters of soursop jelly (*Annona muricata L.*)", *IOP Conf. Ser. Mater. Sci. Eng.,* **736** (2020) 022064.
20. H.C. Mai, T.T.T. Le, T.T. Diep, T.H.N. Le, D.T. Nguyen, L.G. Bach, "Development of solid lipid nanoparticles of gac (*Momordica cocochinensis Spreng*) oil by nanoemulsion technique", *Asian J. Chem.,* **30** (2018) 293–297.
21. S. Fiorito, F. Epifano, V.A. Taddeo, S. Genovese, "Recent acquisitions on oxyprenylated secondary metabolites as anti-inflammatory agents", *Eur. J. Med. Chem.*, **153** (2018) 116–122.
22. S. Rafiq, R. Kaul, S.A. Sofi, N. Bashir, F. Nazir, G.A. Nayik, "Citrus peel as a source of functional ingredient: A review", *J. Saudi Soc. Agri. Sci.,* **17** (2018) 351–358.
23. O. Gulsen, M.L. Roose, "Lemons: diversity and relationships with selected *Citrus* genotypes as measured with nuclear genome markers", *J. Am. Soc. Horti. Sci.,* **126** (2001) 309–317.
24. V.T. Nguyen, M.T. Nguyen, Q.T. Tran, P.V. Thinh, L.M. Bui, T.H.N. Le, V.M. Le, H.T.K. Linh, "Effect of extraction solvent on total polyphenol content, total flavonoid content, and antioxidant activity of soursop seeds (*Annona muricata L.*)", *IOP Conf. Ser. Mater. Sci. Eng.,* **736** (2020) 022063.
25. J. Lücker, M.K.E. Tamer, W. Schwab, F.W.A. Verstappen, L.H.W. van der Plas, H.J. Bouwmeester, H.A. Verhoeven, "Monoterpene biosynthesis in lemon (*Citrus limon*). cDNA isolation and functional analysis of four monoterpene synthases", *Eur. J. Biochem.*, **269** (2002) 3160–3171.

26. M.L. Lota, D. de Rocca Serra, F. Tomi, J. Casanova, "Chemical variability of peel and leaf essential oils of mandarins from *Citrus reticulata* Blanco", *Biochem. Syst. Ecol.,* **28** (2000) 61–78.
27. R. Gao, Q. Zhang, Z. Xu, Z. Wang, G. Chen, X. Deng, C. Fu, W. Cai, "A comparative study on the structural, dielectric and multiferroic properties of $Co_{0.6}Cu_{0.3}Zn_{0.1}Fe_2O_4/Ba_{0.9}Sr_{0.1}Zr_{0.1}Ti_{0.9}O_3$ composite ceramics", *Compos. Part B*, **166** (2019) 204–212.
28. R. Gao, Z. Wang, G. Chen, X. Deng, W. Cai, C. Fu, "Influence of core size on the multiferroic properties of $CoFe_2O_4$@$BaTiO_3$ core shell structured composites", *Ceram. Int.*, **4** (2018) S84–S87.
29. R. Gao, X. Qin, Q. Zhang, Z. Xu, Z. Wang, C. Fu, G. Chen, X. Deng, W. Cai, "Enhancement of magnetoelectric properties of $(1-x)Mn_{0.5}Zn_{0.5}Fe_2O_4$–$xBa_{0.85}Sr_{0.15}Ti_{0.9}Hf_{0.1}O_3$ composite ceramics", *J. Alloys Compd.*, **795** (2019) 501–512.
30. J.R. Macdonald, *Impedance Spectroscopy Emphasizing Solid Materials and Systems,* Wiley, New York, 1987.
31. B.A. Boukamp, "Electrochemical impedance spectroscopy in solid state ionics: Recent advances", *Solid State Ionics*, **169** (2004) 65–73.
32. M.A.L. Nobre, S. Lanfredi, "Dielectric spectroscopy on $Bi_3Zn_2Sb_3O_{14}$ ceramic: An approach based on the complex impedance", *J. Phys. Chem. Solids*, **64** (2003) 2457–2464.
33. K. Prasad, K. Kumari, Lily, K.P. Chandra, K.L. Yadav, S. Sen, "Electrical conduction in $(Na_{0.5}Bi_{0.5})TiO_3$ ceramic: Impedance spectroscopy analysis", *Adv. Appl. Ceram.*, **106** (2007) 241–245.
34. A.K. Jonscher, "A new understanding of the dielectric relaxation of solids", *J. Mater. Sci.*, **16** (1981). 2037–2060.
35. W.H. Jung, J.H. Lee, J.H. Sohn, H.D. Nam, S.H. Cho, "Dielectric loss anomaly in $Ba(Fe_{1/2}Ta_{1/2})O_3$ ceramics", *Mater. Lett.*, **56** (2002) 334–338.
36. K. Prasad, S. Bhagat, Priyanka, K. AmarNath, K.P. Chandra, A.R. Kulkarni, "Electrical properties of $BaY_{0.5}Nb_{0.5}O_3$ ceramic: Impedance spectroscopy analysis", *Phys. B Conden. Matter*, **405** (2010) 3564–3571.
37. Lily, K. Kumari, K. Prasad, K.L. Yadav, "Dielectric and impedance study of lead-free ceramic: $(Na_{0.5}Bi_{0.5})ZrO_3$**",** *J. Mater. Sci.*, **42** (2007) 6252–6259.
38. K. Prasad, S. Bhagat, K. AmarNath, S.N. Choudhary, K.L. Yadav, "Electrical conduction in $Ba(Bi_{0.5}Nb_{0.5})O_3$ ceramic: Impedance spectroscopy analysis", *Mater. Sci. Poland*, **28** (2010) 317–325.
39. R. Maier, J.L. Chon, J.J. Neumeier, L.A. Bendersky, "Ferroelectricity and ferrimagnetism in iron-doped $BaTiO_3$", *Appl. Phys. Lett.*, **78** (2001) 2536–2538.
40. G.D. Sharma, M. Roy, M.S. Roy, "Charge conduction mechanism and photovoltaic properties of 1,2-diazoamino diphenyl ethane (DDE) based schottky device", *Mater. Sci. Eng. B*, **104** (2003). 15–25.
41. M. Nadeem, M.J. Akhtar, A.Y. Khan, R. Shaheen, M.N. Haque, "Ac study of 10% Fe-doped $La_{0.65}Ca_{0.35}MnO_3$ material by impedance spectroscopy", *Chem. Phys. Lett.*, **366** (2002) 433–439.
42. K. Prasad, K.P. Chandra, S. Bhagat, S.N. Choudhary, A.R. Kulkarni, "Structural and electrical properties of lead-free perovskite $Ba(Al_{1/2}Nb_{1/2})O_3$", *J. Am. Ceram. Soc.*, **93** (2010) 190–196.